Mosquito Bite Prevention through Graphene Barrier Layers

Cintia J. Castilho, Dong Li, Muchun Liu, Yue Liu, Huajian Gao*, Robert H. Hurt*

www.pnas.org/cgi/doi/10.1073/pnas.1906612116

Section 1: Characterization of graphene materials.

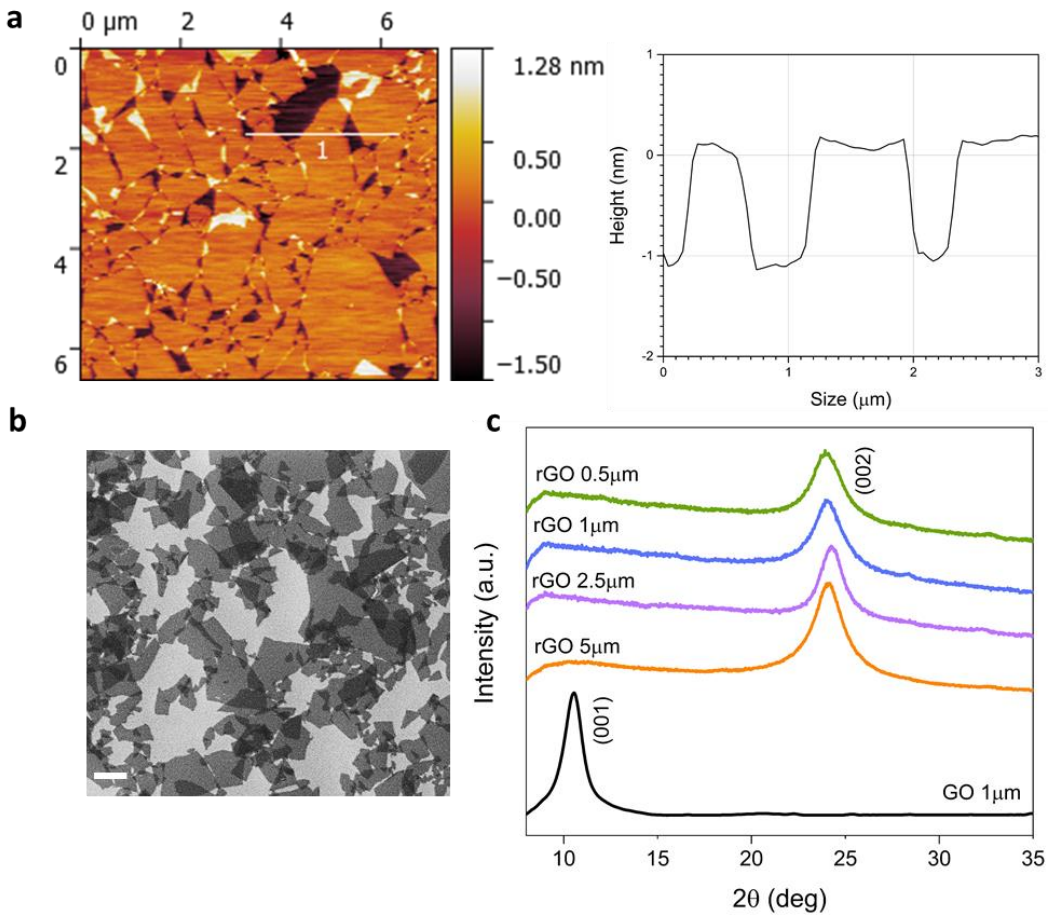

Supplementary Figure S1. Graphene material characterization. **a**, AFM image and height profile of as-produced GO nanosheets. The nanosheets show lateral size of ~1 µm and thickness of ~1 nm. **b**, SEM images of GO nanosheets. Scale bar, 1 µm. **c**, X-ray diffraction patterns of the graphene films used in the live mosquito experiments and puncture tests. The calculated interlayer spacing for rGO films is 0.37 nm and for GO films is 0.84 nm.

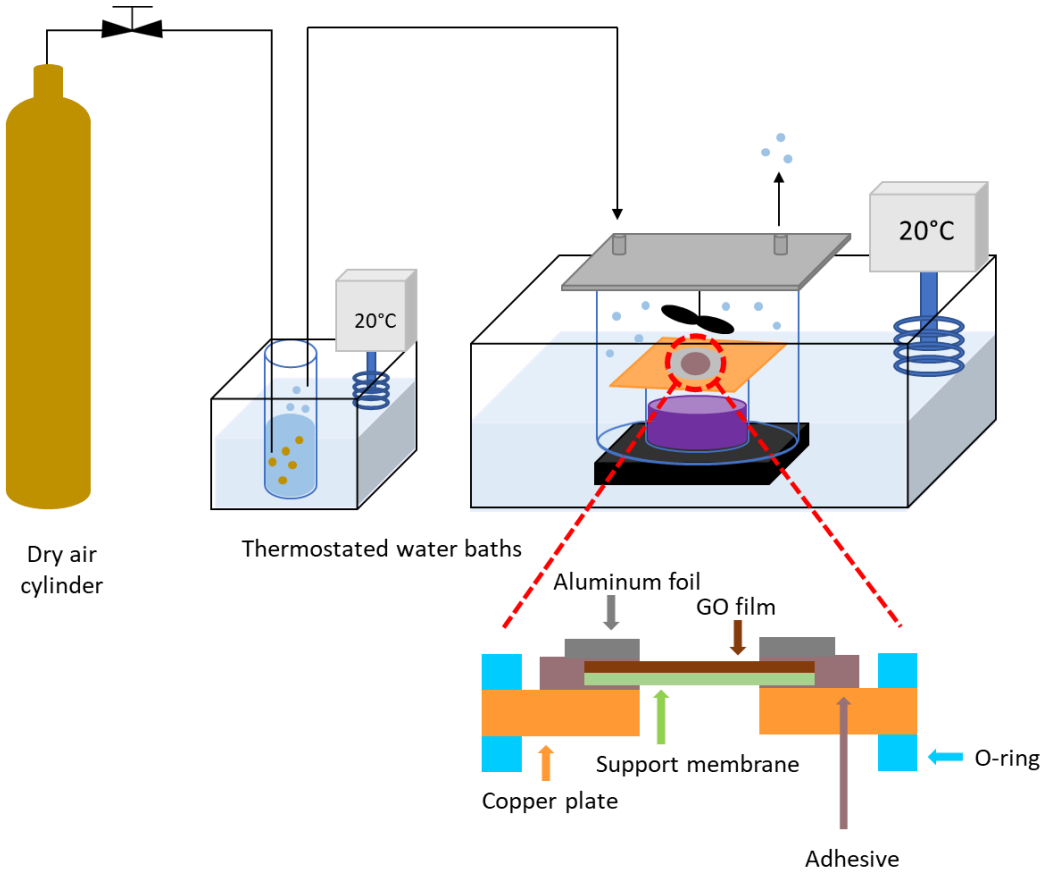

Supplementary Figure S2. Custom-built diffusion cell used for graphene film permeation testing. Top: custom diffusion cell used to test the permeation of vapor molecules through graphene films. Bottom: Details of the graphene film support and system sealing. The device consists of an inner vessel containing the liquid used in the test. The inner vessel is capped with an opened glass cover and a copper plate with a 1 cm hole for the GO films placed in between the vessel and the cover. O-rings are used to further seal the system. An outer vessel creates the simulated atmosphere and is placed in a thermostatic bath to control the temperature during the experiment. The outer vessel is mechanically stirred using a fan while the inner vessel is mechanically stirred using a magnetic stir bar (stir plate is shown in black under the vessels in the figure), ensuring the transport resistances are minimized and only the film resistance is measured. The simulated atmosphere in the outer vessel is created by passing dry air through a column of water. The liquid permeation was measured gravimetrically. The graphene film is supported by a copper plate, and the film is fixed on the plate using an adhesive. A layer of aluminum foil is then used to further seal the system. Liquid hexane is known to be rejected by dry graphene films (1) and thus was used to test the films used in experiments. No mass loss was detected after 6 hours at T = 20°C, confirming the lack of cracks, holes and other defects in the graphene films as well as the quality of the seals in the device.

Section 2: Live mosquito experiments and experimental results

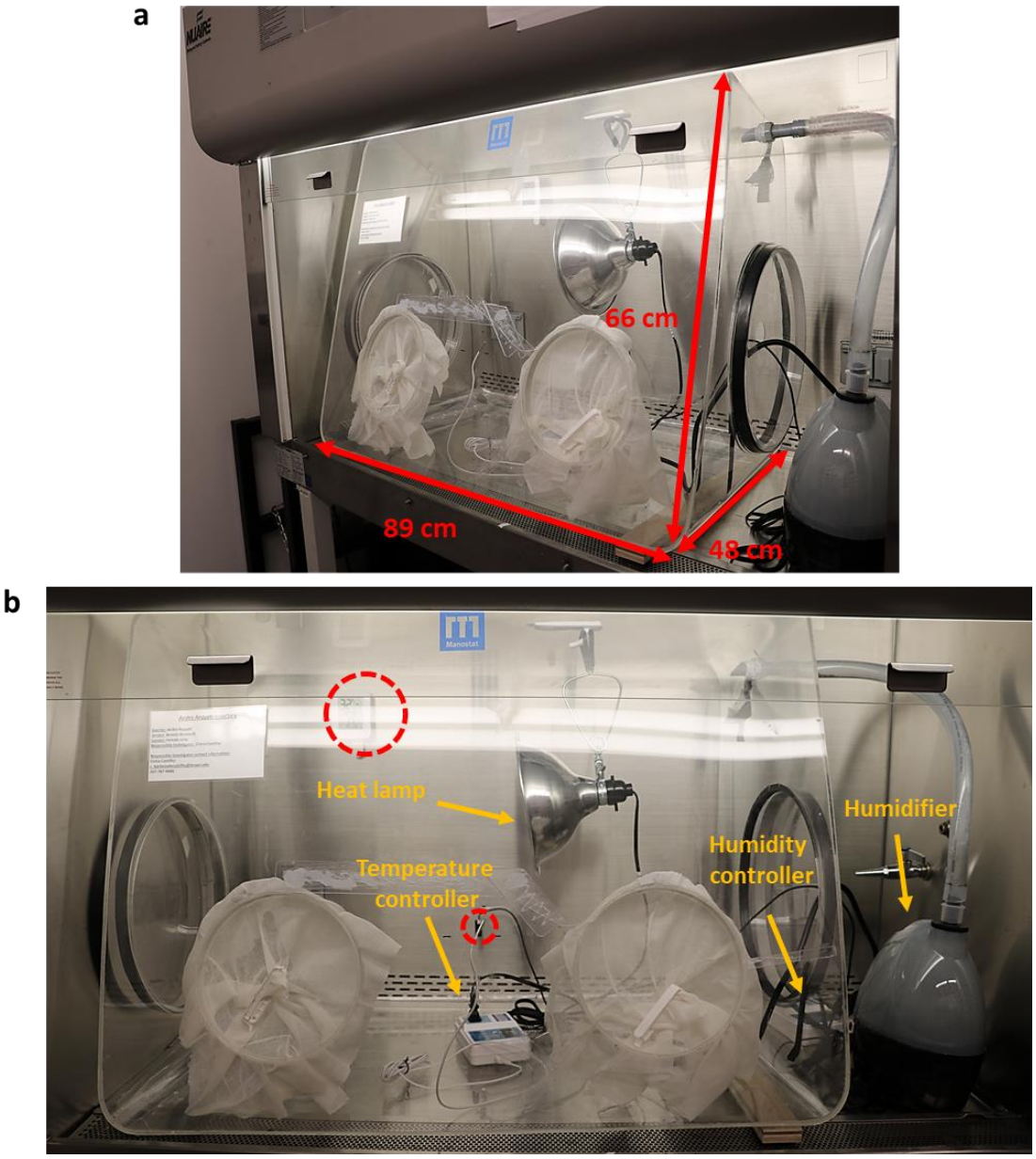

Supplementary Figure S3. Live mosquito experimental apparatus. a) Mosquito enclosure designed from a modified Plexiglas glovebox (see dimensions) placed within a biosafety cabinet. b) Labeled internal contents of the enclosure. The inside temperature was regulated at 27°C ± 2°C by a heat lamp and controller. Humidity was regulated at 75% ± 5% by using a humidifier and controller as described in Imam, et al [2014] (2). The red circles show the humidity and temperature sensors. The original gloves were removed, and the holes converted to access ports for insertion of human arms without release of live mosquitoes. The access ports were outfitted with a cheesecloth cover with a central insertion hole that can be kept closed with a clamp between experiments.

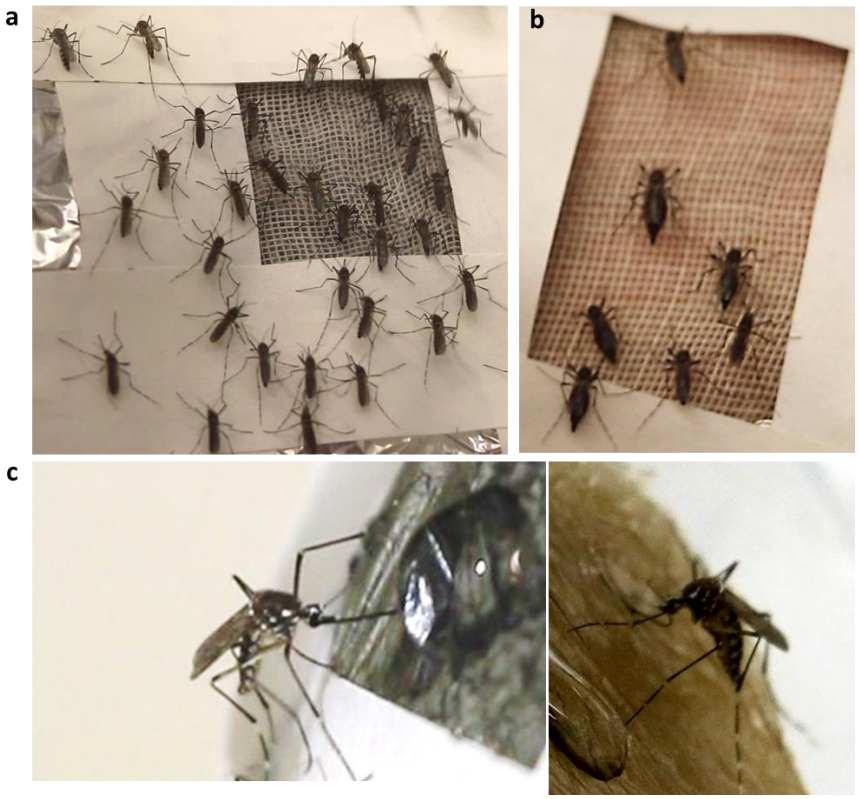

Supplementary Figure S4. Additional example images from live mosquito experiments on human skin patches with graphene coverings. a) Large group of attracted mosquitoes when rGO/cheesecloth films were wetted with human sweat. b) Typical *Aedes* behavior on skin control experiments (no graphene) with cheesecloth overlayer. c) Images of single mosquitoes standing directly on graphene films: (left) on wet rGO films near a sessile water droplet; (right): on wet GO hydrogel films.

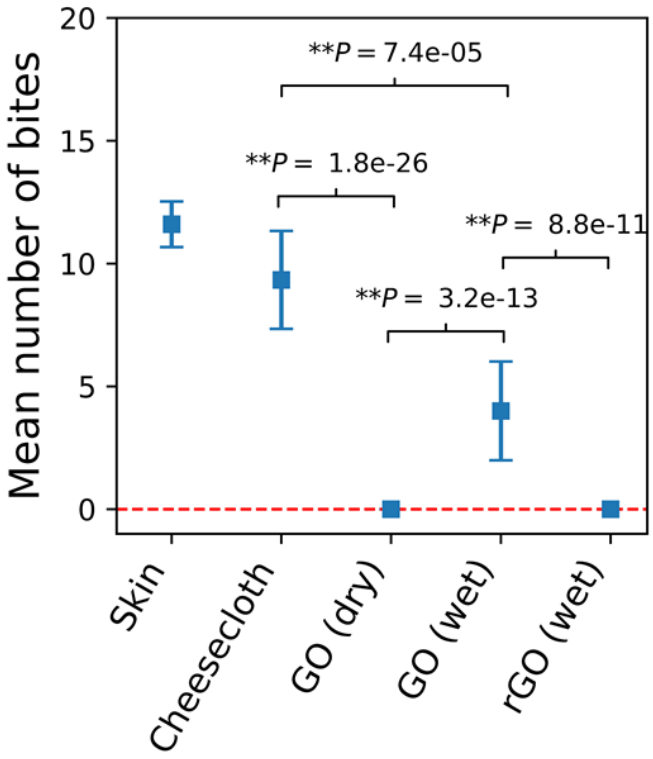

Supplementary Figure S5. **Measured biting statistics with p values calculated from the Poisson distribution model applied to integer count data.** Data are presented as mean number of bites in 5 min ± s.e.m. (n = 4 for rGO (wet); n= 5 for Skin; n = 6 for Cheesecloth and GO (dry); n = 7 for GO (wet)). Statistical significance was calculated using Poisson square root transform. **P <0.001

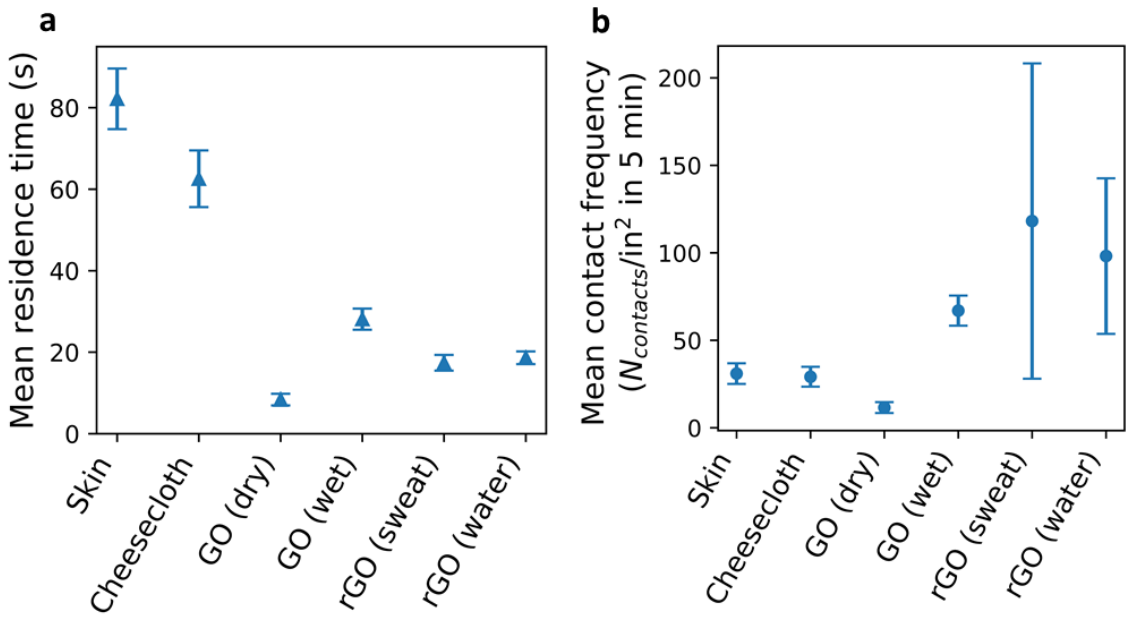

Supplementary Figure S6. Effect of water or sweat addition on mosquito behavior on graphene-covered human skin patches. a, Mean residence times after initial contact on graphene films and control surfaces. **b**, Mean contact frequency of mosquitoes on graphene covered human skin patches and controls.

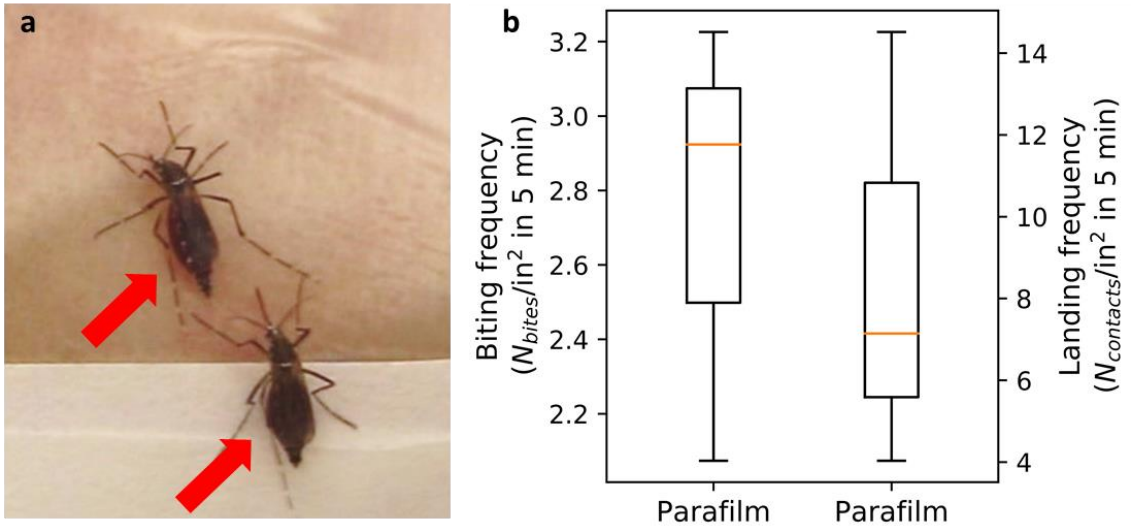

Supplementary Figure S7. **Mosquito biting behavior on parafilm. a,** Typical *Aedes Aegypti* behavior observed during experiments with parafilm. Red arrows show swollen and red abdomen, reflecting successful blood feeding. Thinly stretched parafilm is commonly used in mosquito membrane feeders (3, 4). In those feeders, mosquitoes bite through parafilm to feed on underlying blood. **b,** Quantified mosquito behavior during parafilm experiments. Left axis: Box plot of area-normalized bite frequency on parafilm. Right axis: Box plot of mosquito contact frequency (landings plus walk-ons) on parafilm.

Section 3: Mechanical penetration tests.

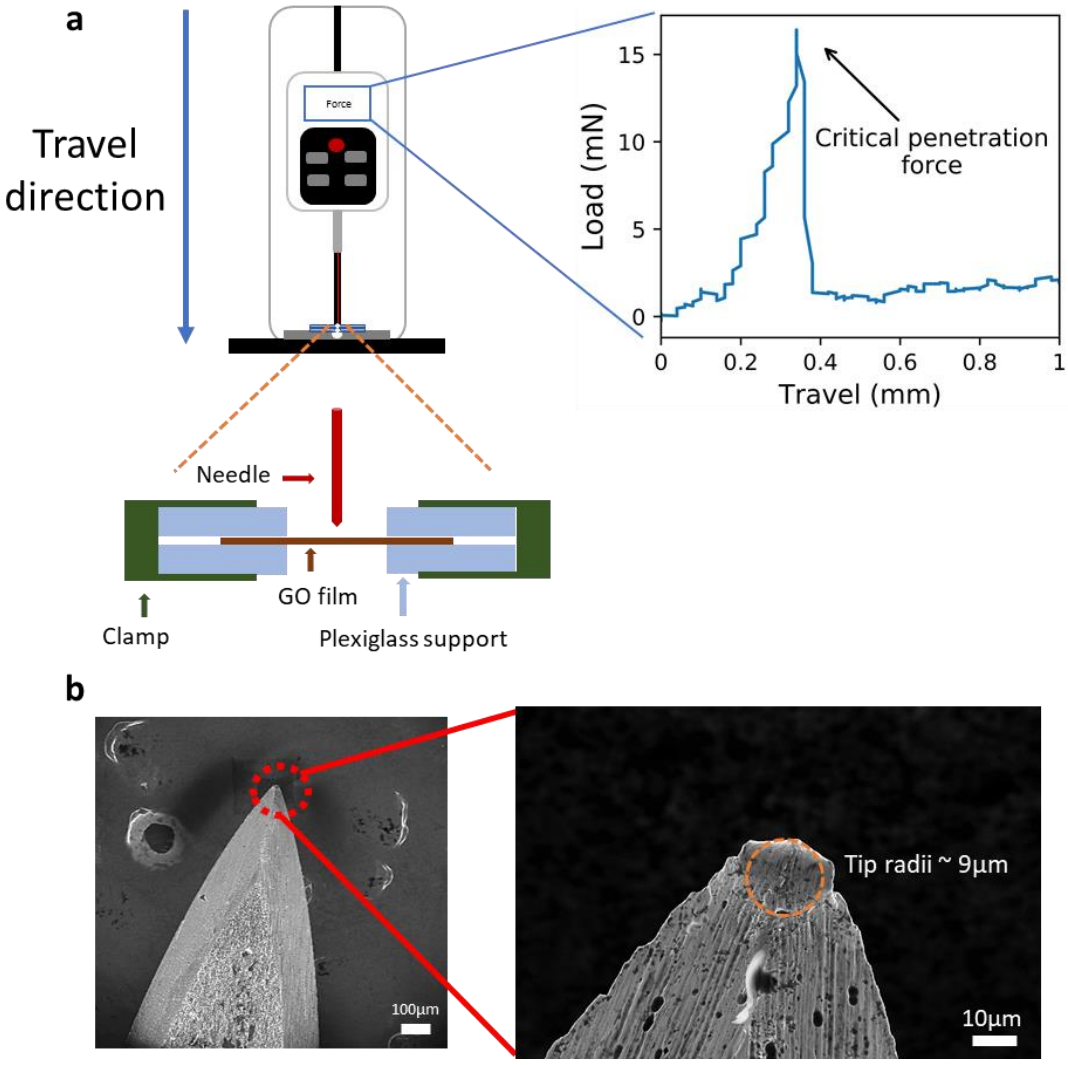

Supplementary Figure S8. **Mechanical puncture test experiments. a**, Sketch of the needle penetration apparatus. The graphene films are clamped between two plexiglass supports with holes of 0.5 cm of diameter. The inset shows an example of the raw data in the form of a force-displacement profile, from which the maximum load is reported as the critical penetration force. **b,** SEM images of the syringe needle tip (stainless steel, 21 gauge) used in the tests (tip radius of curvature ~ 9µm).

Supplementary Note 1: Description of nanoindentation tests on graphene films using Atomic Force Microscopy (AFM).

Free-standing graphene films were prepared as described in methods. The nanoindentation samples were prepared by clamping free standing graphene films (thickness of 0.25 μm – 1 μm) between two thin copper sheets supports. Two different types of AFM tips were used in the nanoindentation tests: a Silicon tip (Asylum research probes) of radius 7 nm and spring constant of 26 N/m and a diamond coated Silicon tip (Nanosensors) of radius 100 nm and spring constant of 6 N/m. The tests were performed in contact mode. The forces exerted by the tips on the films varied from ~0.5 μN to ~5 μN. The films were inspected using the AFM imaging and scanning electron microscopy. No signs of indentation or puncture were found.

Section 4: Mechanical modelling

4.1 Membrane penetration model: the free-standing case

To help understand the mechanical behaviors of GO/rGO paper in the needle penetration experiment, we adopted a theoretical model in which a circular membrane is pressed by a spherical indenter tip at the center (Fig. 4b). The membrane is assumed to be linearly elastic until failure occurs as the maximum tensile stress in the membrane reaches a critical value.

In the membrane penetration model, the following simplifications were made to reduce the complexity of the problem without losing essential features: (1) In modeling the GO/rGO films as a thin membrane, we neglect the effect of bending which is negligible compared to membrane tension (5, 6); (2) The membrane boundary was assumed to be perfectly clamped, which is expected to provide a lower bound to penetration force in case some boundary sliding occurs; (3) The mosquito fascicle and the needle used in experiment (Supplementary Fig. S8) are modeled as having spherical tips, an assumption commonly adopted in contact mechanics of membranes (7-9); (4) The indenter tip was assumed to be rigid as the deformation of the tip is usually negligible compared to that of a flexible membrane.

Even though the size of the indenter tip is much smaller than the membrane radius, it cannot be neglected due to its significant influence on the membrane stress and penetration force. Assuming that the indenter tip has the radius r_t, the membrane can be divided into two regions: the contact region $0 \leq r \leq r_c$ where r_c is the contact radius, and the free region $r_c < r \leq a$ (Fig. 4b). The contact region is loaded by pressure $p(r)$ from the indenter tip, and the outer edge of the free region is clamped.

Supplementary Table 1. Dimensional and dimensionless quantities in the membrane penetration model

Dimensional variables	Dimensionless variables
Radial coordinate r	$\rho = r/a$
Radius of indenter tip r_t	$\rho_t = r_t/a$
Radius of contract area r_c	$\rho_c = r_c/a$
Membrane thickness h	$H = h/a$
Axial deflection w	$W = w/a$
Radial displacement u	$U = u/a$
Stress components σ_r, σ_θ	$S_r = \sigma_r/E$, $S_\theta = \sigma_\theta/E$
Indentation/Penetration force F, F_p	$\bar{F} = F/(Ea^2)$, $\bar{F}_p = F_p/(Ea^2)$
Pressure in contact area P	$P = p/E$

Föppl-Hencky membrane theory (10, 11) is adopted to model the indented membrane. With the introduction of dimensionless variables listed in Supplementary Table 1, the out-of-plane/axial equilibrium equation and compatibility equation can be expressed as (7-9):

$$-HS_r(\rho)\frac{\mathrm{d}W(\rho)}{\mathrm{d}\rho} = \frac{1}{\rho}\int_0^\rho P(\rho)\rho\mathrm{d}\rho, \tag{1}$$

$$\rho\frac{\partial}{\partial\rho}\left\{\frac{1}{\rho}\frac{\partial}{\partial\rho}[\rho^2 S_r(\rho)]\right\} + \frac{1}{2}\left[\frac{\mathrm{d}W(\rho)}{\mathrm{d}\rho}\right]^2 = 0. \tag{2}$$

The normalized circumferential stress component S_θ can be obtained through the in-plane/radial equilibrium equation:

$$S_\theta(\rho) = \frac{\mathrm{d}}{\mathrm{d}\rho}[\rho S_r(\rho)]. \tag{3}$$

The normalized radial displacement U can be calculated as

$$U(\rho) = \rho\varepsilon_\theta(\rho) = \rho[S_\theta(\rho) - \nu S_r(\rho)] \tag{4}$$

where ε_θ is the circumferential strain component and ν is Poisson's ratio of the membrane.

In the contact region $0 \le \rho \le \rho_c$, the normalized membrane deflection W has the following profile:

$$W(\rho) = \bar{d} + \sqrt{\rho_t^2 - \rho^2} \tag{5}$$

where $\bar{d}$ is the normalized downward displacement of the indenter tip. Substituting Eq. (5) into Eq. (2) and integrating the resulting equation twice yield

$$S_r(\rho) = -\frac{\rho_t^2 - \rho^2}{8\rho^2}\ln(\rho_t^2 - \rho^2) + \frac{4c_1 - 1}{8} + \frac{c_2}{\rho^2} \tag{6}$$

where c_1 and c_2 are constants. Since the radial stress component is finite at the center of the membrane, we have condition $S_r(0) < \infty$, which leads to

$$c_2 = \frac{\rho_t^2 \ln \rho_t}{4}. \tag{7}$$

In the free region $\rho_c < \rho \leq 1$, the axial equilibrium equation (1) can be expressed as

$$-HS_r(\rho)\frac{\mathrm{d}W(\rho)}{\mathrm{d}\rho} = \frac{\bar{F}}{2\pi\rho} \tag{8}$$

where the normalized penetration force $\bar{F} = \int_0^{\rho_c} P(\rho) \cdot 2\pi\rho \mathrm{d}\rho$. Combining Eq. (8) and Eq. (2) yields

$$S_r^2(\rho)\rho^3 \frac{\partial}{\partial\rho}\left\{\frac{1}{\rho}\frac{\partial}{\partial\rho}[\rho^2 S_r(\rho)]\right\} = -\frac{1}{8}\left(\frac{\bar{F}}{\pi H}\right)^2. \tag{9}$$

The solution to Eqs. (8) and (9) can be written in the form of polynomial series as

$$W(\rho) = Q^{\frac{1}{3}}\sum_{n=0}^{\infty} a_n\left(1 - \rho^{\frac{4n+2}{3}}\right), \tag{10a}$$

$$S_r(\rho) = \frac{3}{2}Q^{\frac{2}{3}}\sum_{n=0}^{\infty} b_n\rho^{\frac{4n-2}{3}} \tag{10b}$$

where $Q = \bar{F}/(2\pi H)$ is a dimensionless loading variable. $\{a_n\}$ and $\{b_n\}$ are coefficients whose values can be determined through Eqs. (8) and (9) together with the boundary condition at the outer edge of the membrane. For the clamped boundary,

$$U(1) = \left[(1-\nu)\rho S_r(\rho) + \rho^2 \frac{\partial S_r(\rho)}{\partial \rho}\right]_{\rho=1} = 0, \tag{11}$$

and the corresponding values of the first few entries in $\{a_n\}$ and $\{b_n\}$ are listed in Supplementary Table 2.

Supplementary Table 2. Values of coefficient series $\{a_n\}$ and $\{b_n\}$ for different Poisson's ratios

$\nu = 0.17$				$\nu = 0.30$			
a_0	1.817	b_0	5.50×10^{-1}	a_0	1.817	b_0	5.50×10^{-1}
a_1	6.05×10^{-2}	b_1	-5.50×10^{-2}	a_1	1.45×10^{-2}	b_1	-1.31×10^{-2}
a_2	5.18×10^{-3}	b_2	-2.35×10^{-3}	a_2	2.96×10^{-4}	b_2	-1.35×10^{-4}
a_3	5.75×10^{-4}	b_3	-2.00×10^{-4}	a_3	7.87×10^{-6}	b_3	-2.74×10^{-6}
a_4	7.21×10^{-5}	b_4	-2.14×10^{-5}	a_4	2.36×10^{-7}	b_4	-7.00×10^{-8}

At the boundary between the contact and free regions, three continuity conditions should be satisfied:

$$\left[\frac{\mathrm{d}W}{\mathrm{d}\rho}\right]^{-}_{\rho=\rho_c} = \left[\frac{\mathrm{d}W}{\mathrm{d}\rho}\right]^{+}_{\rho=\rho_c}, \tag{12a}$$

$$[W]^{-}_{\rho=\rho_c} = [W]^{+}_{\rho=\rho_c}, \tag{12b}$$

$$[S_r]^{-}_{\rho=\rho_c} = [S_r]^{+}_{\rho=\rho_c} \tag{12c}$$

where $(-)$ and $(+)$ represent quantities on the sides of the contact and free regions, respectively. The conditions (12a-c) are used to determine the values of the normalized contact radius ρ_c, constants $\bar{d}$ in Eq. (5) and c_1 in Eq. (6). Once this is done, the displacement and stress fields in the contact and free regions can be calculated from Eqs. (3-7) and (10).

In the present membrane indentation problem, it turns out that the radial stress component monotonically decreases from the center to the edge of the membrane. Eq. (3) indicates that S_θ is smaller than S_r everywhere except at the center where we have $S_r = S_\theta$. Therefore, the maximum tensile stress in the membrane corresponds to the radial stress at the center. According to the maximum tensile stress criterion, we have

$$S_r(0) \leq S_t \tag{13}$$

where $S_t = \sigma_t/E$ is the normalized tensile strength of the membrane. The corresponding indentation force is taken as the critical penetration force of the membrane.

It can be verified that the above solution to membrane indentation problem converges to classical Schwerin's solution (5) to the indentation of a free-standing membrane under a point load. Supplementary Fig. S9a compares Schwerin's solution, finite element (FE) results and our analytical solution. Relevant FE setups can be found in Section 4.2. Note that FE simulations have convergence problems as the tip radius becomes very small. In Supplementary Fig. S9b, the indentation forces predicted by the analytical solution are in good agreement with the FE results. There is some difference in radial stress in the large deformation regime due to the intrinsic limitations of Föppl-Hencky membrane theory.

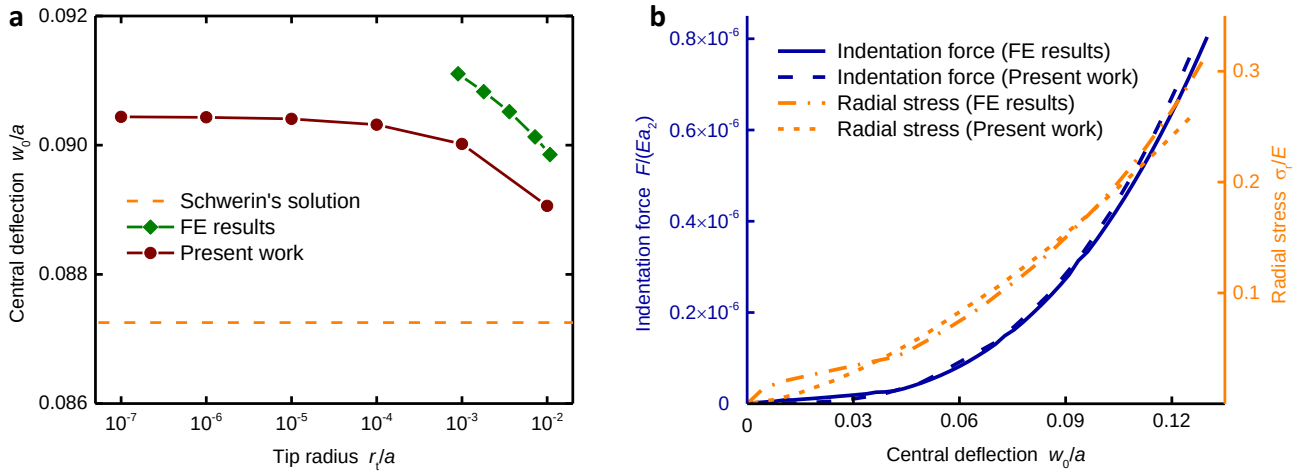

Supplementary Figure S9. Mechanical responses of an indented free-standing membrane. (**a**) Convergence of solutions on membrane deformation as the tip radius goes to zero. (**b**) The profiles of indentation force and central radial stress obtained from the analytical model and FE simulations.

Note that, in the analytical solution, Eqs. (12a-c) do not ensure smoothness in the radial stress and continuity in the radial displacement at the edge of the contact area. The reason is that the polynomial series in Eq. (10) is only an approximate solution to the governing equations. Nevertheless, the present analytical solution should be applicable for the problem in hand since the radial displacement is expected to be very small.

4.2 Effect of substrate

Finite element analysis was performed to investigate the effect of a hyperelastic substrate, which mimics human skin, on the membrane penetration force F_p. An axisymmetric FE model was implemented in ABAQUS (Supplementary Fig. S10a). The bottom of the substrate was fixed, while the lateral boundaries of the substrate and edges of the membrane were kept free. A spherical indenter tip penetrated downward at the center of the membrane. Hard contact in the normal

direction and frictionless interaction in the tangential direction were applied to the interfaces between the tip and the membrane as well as between the membrane and the substrate.

A membrane element with zero bending stiffness was used to model the thin membrane, and the indenter tip was treated as a rigid object. Other model parameters were taken from the needle penetration experiment for dry GO/rGO paper (Supplementary Table 3). The substrate was assumed to obey the following Neo-Hookean constitutive law for an incompressible hyperelastic material:

$$U = C_{10}(\bar{I}_1 - 3) \tag{14}$$

where U is the strain energy per unit volume in the reference configuration, C_{10} is a coefficient associated with the stiffness of the substrate, and $\bar{I}_1 = \bar{\lambda}_1^2 + \bar{\lambda}_2^2 + \bar{\lambda}_3^2$ is the first invariant of the deviatoric strain tensor where $\bar{\lambda}_i, i = 1,2,3$ are deviatoric principal stretches in the substrate. The stiffness coefficient of stratum corneum of human skin $C_{10} = 13.8$ MPa (12) was used in this study. The free-standing membrane model serves as a reference.

Supplementary Table 3. Parameters in the needle penetration tests and membrane indentation model.

	Young's modulus (GPa)	Poisson's ratio	Membrane thickness (μm)	Membrane radius (mm)	Tip radius (μm)
GO paper	2.28*	0.17†	0.5–5.0	2.5	9.0
rGO paper	2.55*	0.17†	0.5–5.0	2.5	9.0

* Obtained by fitting experimental data
† Values reported in literature(13)

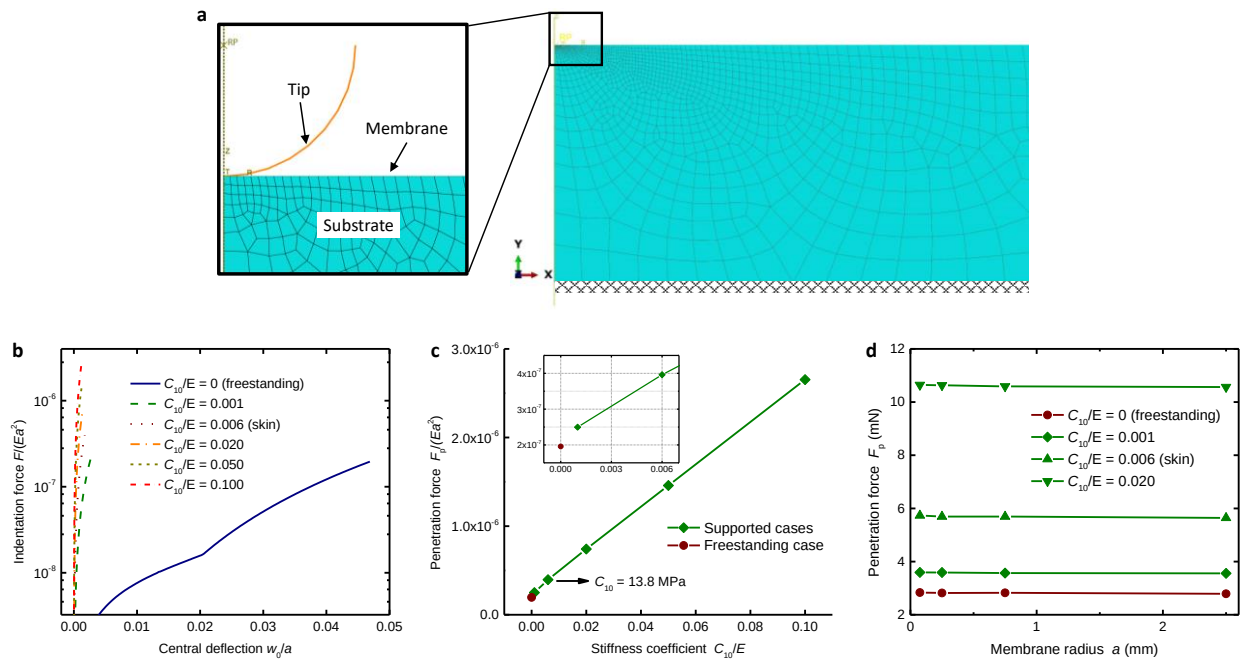

Supplementary Figure S10. Effects of a hyperelastic substrate on the penetration force of a thin membrane. (**a**) The FE model of the tip-membrane-substrate system (**b**) Indentation force profiles for different substrate stiffness coefficients. The cases $C_{10} = 0$ and $C_{10}/E = 0.006$, where E is the Young's modulus of the membrane, correspond to the cases without and with substrate support mimicking human skin, respectively. Artificial stiffness coefficients are used in other cases. (**c**) Penetration forces for different substrate stiffness coefficients. The inset shows details of the main figure when C_{10} is small. The membrane thickness is assumed to be $h/a = 0.002$, where a is the membrane radius, in all cases in (**b**) and (**c**). (**d**) Variations of penetration force with truncations on the membrane size.

Supplementary Fig. S10b shows the comparison between the free-standing membrane case and supported membrane cases with the membrane tensile strength taken to be $\sigma_t/E = 0.05$. Compared to the case of a free-standing membrane, the substrate is found to reduce the central membrane deflection to $1/16$ or less in all supported membrane cases. The corresponding penetration forces are plotted in Supplementary Fig. S10c. The freestanding membrane case has the lowest penetration force, implying that the membrane without support of substrate is the most vulnerable to penetration by a sharp tip. The penetration force for supported cases decreases approximately linearly with the stiffness coefficient C_{10} of the substrate, and the point representing the free-standing case also lies close to the line. In particular, the penetration resistance of the thin

membrane on human skin is almost twice that in the free-standing case. Supplementary Fig. S10d confirms that the predicted penetration force is not sensitive to the selected membrane radius in the model as along as the membrane radius is sufficiently large.

4.3 Effect of Poisson's ratio

In our FE simulations and theoretical analysis, we have taken the Poisson's ratio of GO/rGO paper to be $\nu = 0.17$ (13). It can be shown that the detailed choice of ν will not significantly affect our conclusions.

Different Poisson's ratios are considered in both FE and theoretical models of the free-standing membrane case (Supplementary Fig. S11). The relationships between indentation force and central deflection are shown under the membrane tensile strength of $S_t = 0.19$ in Supplementary Fig. S11a. It can be seen that the differences in central deflection between Poisson's ratios $\nu = 0.1$ and $\nu = 0.4$ are less than 10% in both FE and theoretical results.

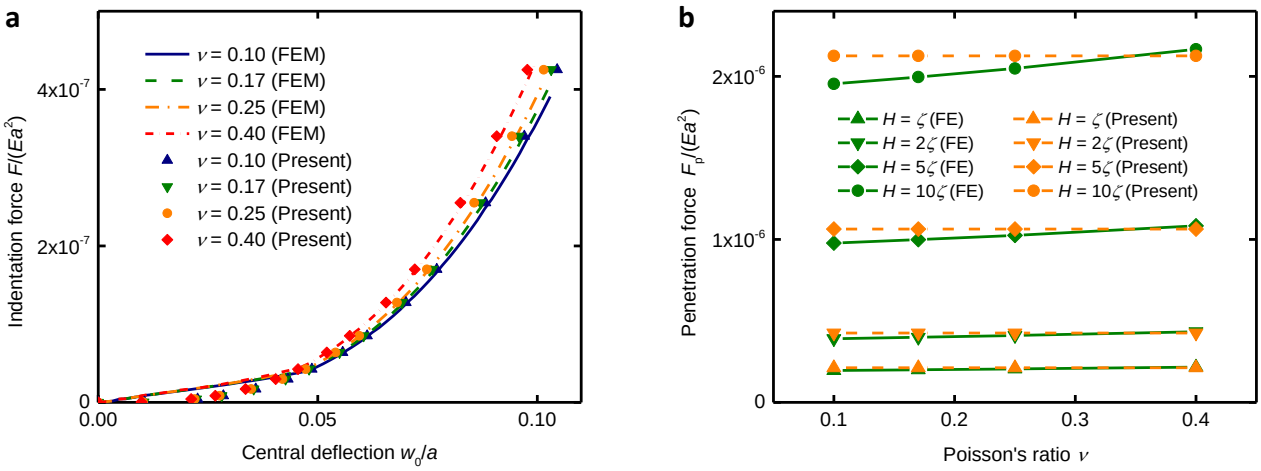

Supplementary Figure S11. Effect of Poisson's ratio on mechanical responses of a free-standing membrane under indentation. (**a**) Indentation force profiles for different Poisson's ratios. The normalized membrane thickness is taken as $H = h/a = 2\zeta$ where $\zeta = 2 \times 10^{-4}$ is the reference thickness. (**b**) Effect of Poisson's ratio on the penetration force for different membrane thicknesses.

Supplementary Fig. S11b shows that the penetration forces do not exhibit significant dependence on Poisson's ratio. Similar behavior can also be found in the FE results for membrane thicknesses of $H = \zeta$ and 2ζ, whereas the penetration forces increase gently with Poisson's ratios for relatively large thicknesses of $H = 5\zeta$ and 10ζ. However, the increases in penetration force are all within 10% compared with the results for $\nu = 0.1$.

4.4 Fitting Young's modulus of GO/rGO paper

Another uncertain material parameter is Young's modulus of GO/rGO paper which can vary in a broad range due to different preparation conditions(14-17). In principle, the exact value of Young's modulus of GO/rGO paper should be estimated by fitting with experiment. Here, we utilize the membrane penetration model to estimate the Young's modulus of GO/rGO paper from the needle penetration experiment data.

In the force profile of a GO paper sample shown in Supplementary Fig. S12a, an abrupt increase in indentation force indicates that the loading process starts from the contact between the indenter tip and the membrane and ends with the failure of the membrane. While it is difficult to identify when the indenter tip touches the membrane surface, we take advantage of the predicted scaling law between the indentation force F and membrane central deflection w_0. For a thin membrane, the indentation force scales with the central deflection as (5, 8)

$$\frac{F}{Ea^2} = g(E, \nu, a, h, r_t)\left(\frac{w_0}{a}\right)^{\xi} \tag{15}$$

where $\xi = 3$ and the function g depends on material and geometrical parameters of the membrane as well as the tip radius. Our membrane penetration model and FE simulations (Supplementary Fig. S9b) also support this scaling law with $\xi = 3.01$ and $\xi = 2.94$, respectively. Therefore, for each force profile, we can adjust the starting point for the loading process such that it fits well with the cubic scaling law (Supplementary Fig. S12).

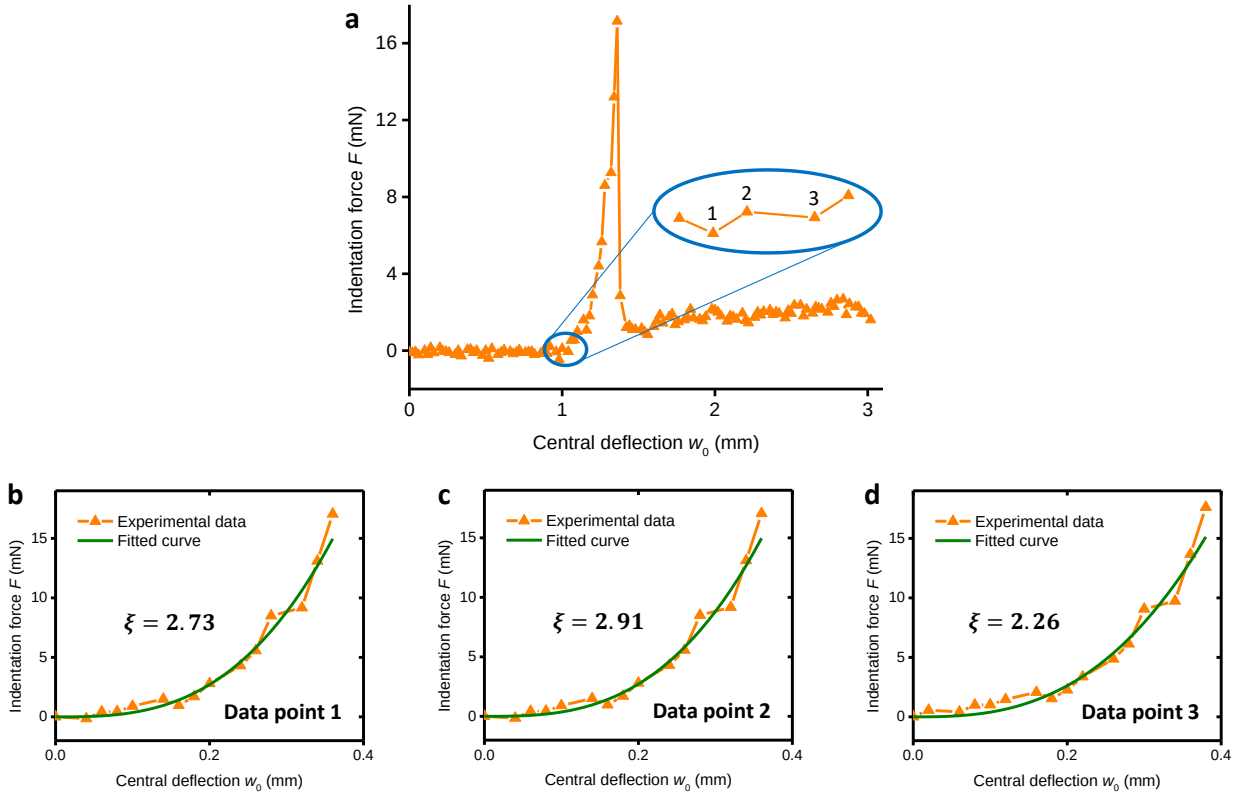

Supplementary Figure S12. Scaling laws in the indentation force profile from the needle penetration experiment. (**a**) Force profile for GO paper with thickness $h = 1$ μm. Data points 1, 2, 3 are three potential starting points of the loading process. (**b-d**) Loading processes with points 1, 2, 3 taken as starting points, respectively. The exponents ξ are obtained by fitting experimental data with Eq. (15). Point 2 with $\xi = 2.91$ is the closest point to the true starting point of the loading process.

After the range of the loading process has been determined, the experimental data of indentation force versus central deflection can be used to estimate the Young's modulus of GO/rGO paper through the following least square fitting:

$$\text{Find} \quad E_{\text{fit}}$$

$$\text{Min.} \quad S = \sum_{i=1}^{k} [w_{0i}^{*} - w_0(F_i^{*}; E_{\text{fit}})]^2$$

$$\text{s.t.} \quad w_0 = M(F), \ i = 1, \ \ldots k$$

where E_{fit} denotes the fitted Young's modulus and S denotes the sum of squared residue between measured and calculated values for the central deflection. (F_i^*, w_{0i}^*) represents the i-th pair of indentation force versus central deflection data extracted from experiment, and k is the number of data points in the loading process. The central deflection of the membrane w_0 in response to the indentation force F is predicted by the membrane penetration model denoted as $M(\cdot)$. The final value of Young's modulus is taken as the average of fitted values for samples with different thicknesses. The fitting results of Young's modulus for GO/rGO paper are listed in Supplementary Table 3.

Section 5: Characterization of graphene films in the dry and wet states

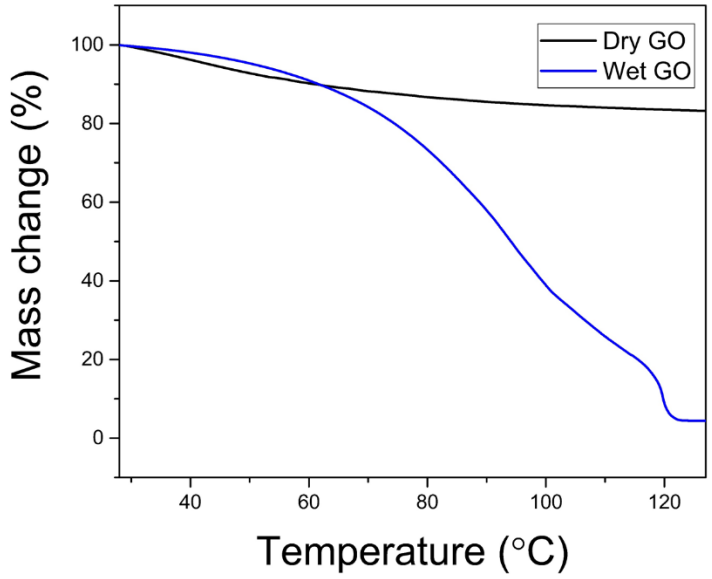

Supplementary Figure S13. TGA data on thermal mass loss for graphene oxide films in the dry and wet states. The "dry" GO films are those equilibrated with laboratory air (51% relative humidity), and contain about 20 wt-% water. The "wet" GO films were created by placing dry films (2.5 µm thickness, 4 cm^2 area) in direct contact with excess liquid water (500 µL) and the surface water removed by blotting with a laboratory tissue. These wet GO films contain 96 wt-% water, which implies swelling to a thickness of approximately 30 µm.

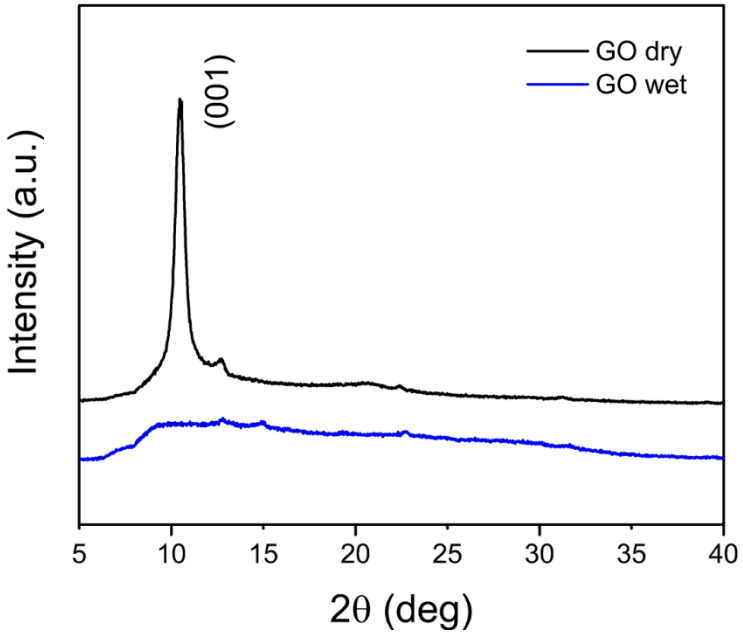

Supplementary Figure S14. XRD characterization of the graphene films in the dry and wet states. The interlayer spacing for dry GO films is 0.83 nm by the Bragg equation. The wet films (made as described

in Fig. S13) do not show an XRD peak, consistent with the behavior of other GO films in the presence of excess liquid water (18).

References – Supplementary Information Section

1. Nair RR, Wu HA, Jayaram PN, Grigorieva IV, & Geim AK (2012) Unimpeded Permeation of Water Through Helium-Leak–Tight Graphene-Based Membranes. *Science* 335(6067):442-444.
2. Imam H, Z, Sofi G, & Aziz S (2014) The basic rules and methods of mosquito rearing (*Aedes aegypti*). *Tropical Parasitology* 4(1):53-55.
3. Finlayson C, Saingamsook J, & Somboon P (2015) A simple and affordable membrane-feeding method for Aedes aegpyti and Anopheles minimus (Diptera: Culicidae). *Acta tropica* 152:245-251.
4. Gonzales K & Hansen I (2016) Artificial diets for mosquitoes. *International journal of environmental research and public health* 13(12):1267.
5. Komaragiri U, Begley M, & Simmonds J (2005) The mechanical response of freestanding circular elastic films under point and pressure loads. *Journal of applied mechanics* 72(2):203-212.
6. Vella D & Davidovitch B (2017) Indentation metrology of clamped, ultra-thin elastic sheets. *Soft Matter* 13(11):2264-2278.
7. Bhatia NM & Nachbar W (1968) Finite indentation of an elastic membrane by a spherical indenter. *International Journal of Non-Linear Mechanics* 3(3):307-324.
8. Begley MR & Mackin TJ (2004) Spherical indentation of freestanding circular thin films in the membrane regime. *Journal of the Mechanics and Physics of Solids* 52(9):2005-2023.
9. Jin C, Davoodabadi A, Li J, Wang Y, & Singler T (2017) Spherical indentation of a freestanding circular membrane revisited: Analytical solutions and experiments. *Journal of the Mechanics and Physics of Solids* 100:85-102.
10. Föppl A (1910) *Vorlesungen über technische Mechanik* (BG Teubner).
11. Hencky H (1915) Uber den Spannungszustand in kreisrunden Platten mit verschwindender Biegungssteifigkeit. *Zeitschrift fur Mathematik und Physik* 63:311-317.
12. Kong XQ & Wu CW (2009) Measurement and Prediction of Insertion Force for the Mosquito Fascicle Penetrating into Human Skin. *Journal of Bionic Engineering* 6(2):143-152.

13. Ranjbartoreh AR, Wang B, Shen X, & Wang G (2011) Advanced mechanical properties of graphene paper. *Journal of Applied Physics* 109(1):014306.
14. Dikin DA, *et al.* (2007) Preparation and characterization of graphene oxide paper. *Nature* 448(7152):457.
15. Pei S, Zhao J, Du J, Ren W, & Cheng H-M (2010) Direct reduction of graphene oxide films into highly conductive and flexible graphene films by hydrohalic acids. *Carbon* 48(15):4466-4474.
16. Lin X, *et al.* (2012) Fabrication of highly-aligned, conductive, and strong graphene papers using ultralarge graphene oxide sheets. *ACS nano* 6(12):10708-10719.
17. Wang C, Frogley MD, Cinque G, Liu L-Q, & Barber AH (2013) Deformation and failure mechanisms in graphene oxide paper using in situ nanomechanical tensile testing. *Carbon* 63:471-477.
18. Chen P-Y, *et al.* (2016) Hierarchical Metal Oxide Topographies Replicated from Highly Textured Graphene Oxide by Intercalation Templating. *ACS Nano* 10(12):10869-10879.